

On the feasibility of analog fiber dispersion-based photonic beamforming for mmWave wireless access over 100GHz DWDM grids

Original

On the feasibility of analog fiber dispersion-based photonic beamforming for mmWave wireless access over 100GHz DWDM grids / Vujcic, Z., Gelabert, X., Santos, M.C., Méndez, R., Gaudino, R.. - In: JOURNAL OF OPTICAL COMMUNICATIONS AND NETWORKING. - ISSN 1943-0620. - 17:11(2025), pp. 70-81. [10.1364/jocn.567208]

Availability:

This version is available at: 11583/3010862 since: 2026-05-15T13:34:36Z

Publisher:

Optica Publishing Group

Published

DOI:10.1364/jocn.567208

Terms of use:

This article is made available under terms and conditions as specified in the corresponding bibliographic description in the repository

Publisher copyright

Optica Publishing Group (formely OSA) postprint versione editoriale con OAPA (OA Publishing Agreement)

© 2025 Optica Publishing Group. Users may use, reuse, and build upon the article, or use the article for text or data mining, so long as such uses are for non-commercial purposes and appropriate attribution is maintained. All other rights are reserved.

(Article begins on next page)

On the feasibility of analog fiber dispersion-based photonic beamforming for mmWave wireless access over 100 GHz DWDM grids

ZORAN VUJICIC,^{1,*}  XAVIER GELABERT,² MARIA C. SANTOS,³ RODRIGO MÉNDEZ,³ 
AND ROBERTO GAUDINO⁴ 

¹Instituto de Telecomunicações, DETI, Universidade de Aveiro, 3810-193 Aveiro, Portugal

²Huawei Technologies Sweden AB, Stockholm Research Centre, 16440 Kista, Sweden

³Universitat Politècnica de Catalunya, Signal Theory and Communications Department, 08034 Barcelona, Spain

⁴Politecnico di Torino, Dipartimento di Elettronica e Telecomunicazioni (DET), 10129 Turin, Italy

*zvujicic@av.it.pt

Received 19 May 2025; revised 10 August 2025; accepted 18 August 2025; published 17 September 2025

We investigate the spectral coexistence feasibility of analog optically driven mmWave antenna beamforming over dispersive fiber links within standardized dense wavelength-division multiplexing (DWDM) grids, targeting next-generation wireless mobile network broadband use cases. Our analysis focuses on integration with legacy passive optical network (PON) infrastructure, using three representative deployment scenarios to evaluate compatibility under practical spectral constraints. We present a use case-driven spectral feasibility assessment of analog radio-over-fiber (ARoF)-based mmWave beam steering over DWDM grids, using a numerical framework that evaluates beamwidth requirements under link distance, carrier frequency, as well as fiber and component spectral constraints. We demonstrate that ARoF carrier frequency optimization, governed by WDM grid and component spectral tolerances, enables optimized beam steering resolution. © 2025 Optica Publishing Group under the terms of the [Optica Open Access Publishing Agreement](#)

<https://doi.org/10.1364/JOCN.567208>

1. INTRODUCTION

Dynamic beam steering is essential for 6G systems leveraging mmWave and THz bands to meet rising demand. High path loss and blockage in dense environments require adaptive, directional beams with real-time user tracking [1,2]. Integrated sensing and communication systems intensify the need for precise beam control [3]. Beam steering also supports spatial multiplexing, interference suppression, and diversity. Fiber-optic links offer high-capacity, low-loss connectivity in centralized architectures, decoupling processing from antenna front-ends for scalable, energy-efficient, dense deployments [4]. Analog radio-over-fiber (ARoF) architectures streamline this model by eliminating digitization at remote radio heads (RRHs), reducing latency, power, and complexity while preserving RF bandwidth and phase [5].

Phased array antennas (PAAs) are widely adopted for electronic beam steering without mechanical motion, achieved by applying relative delays across antenna elements (AEs) via beamforming networks (BFNs), typically employing electronic phase shifters suffering from frequency-dependent beam squint [6]. True-time delay (TTD) techniques mitigate squint but tend to be narrowband, lossy, and power-hungry [7]. High directivity without grating lobes requires high PAA element

counts, adding complexity [8,9]. To address these limitations, microwave photonics enables wideband TTD-based optical BFNs (OBFNs) by leveraging electromagnetic interference immunity, multiplexing, low-loss, and ultra-wide bandwidth, while supporting passive, fiber-fed RRHs for scalable, high-performance wireless networks [10].

Photonic TTD OBFNs using optical tunable delay lines (OTDLs) have been widely studied [11]. Compact, CMOS-compatible photonic integrated circuits (PICs) have been demonstrated on passive silicon-on-insulator (SOI) and silicon nitride platforms, with hybrid indium phosphide developments enabling co-integration of active elements. Two main OTDL types stand out: optical ring resonators (ORRs), offering large delays in compact footprints through resonant light recirculation but with constrained bandwidth, and switched delay lines based on Mach-Zehnder interferometers (MZIs). Tunability is typically achieved via the thermo-optic effect, with MZIs also supporting electro-optic tuning for faster switching [11]. These OBFNs usually operate at a single fixed wavelength per beam and require active elements to be placed at the RRH for beam steering. While wavelength tuning can enable centralized, passive RRH configurations [12,13], such approaches still demand precise signal path adjustment and

beamforming hardware at the RRH, adding complexity and limiting scalability.

Supported by advances in optical frequency comb (OFC) sources and multiwavelength lasers, multi- λ OBFNs address these issues by assigning a unique λ to each AE (λ -to-AE), enabling centralized beam control with simple demultiplexing at the RRH. Numerous fixed- λ -to-AE solutions using tunable delay structures have been explored: ORRs [14], chirped fiber Bragg gratings (CFBGs) [15,16], temperature-tuned etalon filters [17], switched OTDLs [18,19], pre-selectable delays [20], and programmable delay elements [21,22]. Tuning within wavelength-division multiplexing (WDM) bands per AE enables centralized beamforming with fixed delay elements, leveraging precise tunable lasers and high-count OFCs with up to 81 C-band channels [23], improving beam control accuracy, stability, and performance. Most implementations rely on fixed delay gradient elements comprised of CFBGs [24–26], etalon filters [27], or standard single-mode fiber (SSMF) links from the central office (CO) to RRHs [23,28–31]. Architectures leveraging SSMF chromatic dispersion (CD) are advantageous as they require no additional beamforming hardware, including at the CO. Following this principle, we focus on λ -to-AE systems where a simplified RRH relies on passive optical filtering to map distinct ARoF wavelength channels to each AE, allowing centrally controlled dynamic beam steering. The fundamental viability of this paradigm has been confirmed by several physical-layer demonstrations. Complete ARoF links have successfully integrated multi- λ sources to achieve wireless data transmission with beam steering [28,30]. These proofs-of-concept have validated the principle at mmWave frequencies (i.e., 25 and 60 GHz) over multi-km fiber spans, establishing a foundation for the analysis of larger-scale network implementations.

These demonstrations, however, leverage fiber transmission with no stringent spectral constraints, thus overlooking associated impacts in scenarios of coexistence with legacy passive optical networks (PONs). To our knowledge, there remains a lack of systematic analysis focused on constraints specific to standardized PON dense WDM (DWDM) grids. Moreover, a use-case-based analysis is required as the system architecture must match the conditions specific to the wireless transmission band, coverage, steering range, and latency.

This paper addresses the gap by presenting a feasibility study under spectral constraints imposed by standardized 100 GHz DWDM grids on generalized CD-based λ -to-AE architectures, evaluated against key radio network parameters. The aim of this work is to establish the upper-bound beamforming performance under these limitations, creating a benchmark applicable across a range of implementation specifics. As this analysis is complementary to ARoF signal performance-oriented studies, it isolates the impact of spectral constraints from other system performance limitations in the ARoF segment. Thus, the impacts of optical power budget, nonlinear effects, and inter-channel crosstalk are acknowledged but lie outside the scope of this work. Finally, this work proposes optimization strategies for balancing enhanced beamforming performance against reduced RRH complexity. To ground this assessment, we analyze three diverse high-capacity mmWave access scenarios, chosen to reflect the demands

of fixed broadband, immersive media, and dense indoor networks.

The paper is structured as follows: Section 2 presents the theoretical basis for spectral efficiency optimization in λ -to-AE architectures, and a feasibility assessment numerical framework is detailed in Section 3. Section 4 analyzes 6G mmWave use cases, while Section 5 concludes the work.

2. BEAMFORMING IN mmWave DISPERSIVE FIBER LINKS

To establish the phase shift and optical fronthaul requirements, we consider 1D and 2D antenna arrays with L elements for analog 2D and 3D beamforming, respectively, as represented in Fig. 1. These correspond to the uniform linear arrays (ULAs) with $L = N$ elements and uniform planar arrays (UPAs) with $L = N \times M$ antenna elements, respectively. We hereby adopt the terminology as provided in [32], along with the spherical coordinate convention therein, whereby the azimuth $\varphi \in [-\pi, \pi]$ and elevation $\theta \in [-\pi/2, \pi/2]$ angles are measured as shown in Fig. 1. In a generalized scenario, we consider 3D beamforming using a rectangular UPA operating at wavelength λ_c , with inter-element spacing d equal in both directions, $d = d_x = d_y$, and set to satisfy the condition for elimination of grating lobes: $d = \lambda_c/2$ [32]. The array phase progression $\Delta\phi$, representing the differential phase shift applied between adjacent antenna elements to steer the beam in a desired direction (φ, θ), takes two distinct values for azimuth ($\Delta\phi_{az}$) and elevation ($\Delta\phi_{el}$) to control the beam in both planes [33,34]. For simplicity, in considering a ULA for 2D beamforming in azimuth, we assume $\theta = 0$. The beam steering granularity and flexibility depend on the ability to generate narrow beams, which in turn dictates the minimum number of antenna elements L required for adequate resolution and coverage. In λ -to-AE beamforming systems relying on legacy DWDM grids without remote deployment of TTD elements, this requirement imposes optical spectrum constraints.

Figure 2 illustrates the operating principle of an ARoF-based λ -to-AE architecture for centralized mmWave antenna beamforming. L radio signals generated by the baseband units (BBUs) located at a CO are transmitted to the RRHs at the antenna sites via ARoF transport architecture, supporting centralization. For illustrative purposes, the figure assumes a ULA configuration ($\theta = 0$). We consider multiple variants of transmitter and receiver architectures for mmWave ARoF signal generation and detection. Two key approaches are highlighted in the Fig. 2 insets: (a) transmitter electrical upshifting (TEU), in which baseband signals are electrically upconverted to the target RF frequency, and (b) heterodyne detection-based upshifting (HDU), where the mmWave signal is generated through photonic frequency mixing at the photodetector (PD). For HDU, an optical comb generator (OCG) ensures phase coherence between optical tones necessary for effective heterodyne detection. As shown in Fig. 2, we hereby assume single-sideband modulation of the radio signal, as it allows improved spectral efficiency and mitigation of CD-induced radio amplitude fading. However, more cost-effective double-sideband modulation has been successfully demonstrated

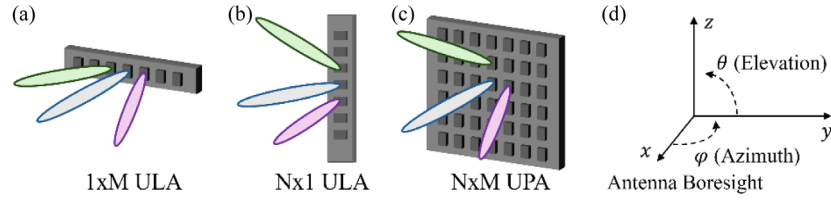


Fig. 1. Beamforming from 2D (a) a horizontal ULA in azimuth and (b) a vertical ULA in elevation. (c) 3D beamforming from a UPA, with directivity in both the vertical and horizontal planes. (d) The adopted spherical coordinate convention. The beams are illustrative, showing possible directions when one is active at a time, and only main lobes are shown. Although drawn here from single elements for clarity, beams are synthesized by phase control across the full array.

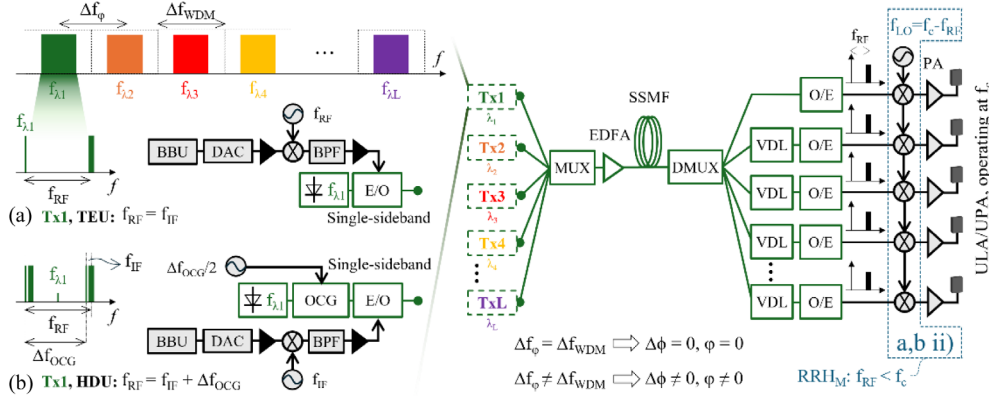


Fig. 2. Remote DWDM-based optical beamforming system supporting L antenna elements, considering (a) TEU-based and (b) HDU-based mmWave ARoF system architectures. Electrical mixers at the antenna site indicate the RRH_M case where $f_{RF} < f_c$. Tx, transmitter; E/O, electrical-to-optical conversion; DAC, digital-to-analog converter; BPF, bandpass filter; EDFA, erbium-doped fiber amplifier; and E/O, optical-to-electrical conversion.

in practical implementations [18,23,28–31], introducing a trade-off between cost and performance that depends on the level of chromatic dispersion required for a given application as well as on spectral availability. The L ARoF channels are wavelength-division multiplexed (MUX), transmitted over SSMF, and demultiplexed (DMUX) at the RRH, while conforming to a legacy DWDM grid. Each optical signal is detected by a PD and fed directly to its respective AE input in an antenna array with beamforming capabilities. Figure 2 also accounts for cases where the generated f_{RF} differs from the final, air-interface mmWave carrier frequency f_c , with optional RF mixers included in the chain to accommodate such scenarios. To ensure precise beam directionality, variable delay lines (VDLs) are employed to synchronize the RF phases of the ARoF signals such that, under nominal WDM channel spacing Δf_{WDM} , the array radiates a beam at $\varphi = 0^\circ$. It is of note that delay adjustment elements may be placed at the CO, for further RRH simplification [20]. When the channel spacing deviates from Δf_{WDM} , CD in the SSMF introduces differential phase shifts among the ARoF signals, resulting in a beam steering angle of $\varphi \neq 0^\circ$. Such photonics-assisted remote beamforming architecture offers a key advantage in enabling high-speed, fully centralized beam steering without the need for active RF electronics or digital signal processing (DSP) at the antenna site. Although the inclusion of electrical mixers at the antenna site ($f_{RF} < f_c$) offsets low RRH complexity, we highlight this configuration as relevant in PON coexistence

scenarios where opto-electronic bandwidth and fiber spectral availability are constrained.

Assuming that adjacent multiplexed ARoF signals are data modulated at the RF frequency f_{RF} using optical carriers spaced in wavelength by $\Delta\lambda$, the relative group delay $\Delta\tau$ they experience upon propagation through an SSMF, characterized by length L_{SSMF} and dispersion parameter D , yields the RF phase shift of $\Delta\phi = 2\pi f_{RF} \cdot \Delta\tau = 2\pi f_{RF} \cdot D \cdot L_{SSMF} \cdot \Delta\lambda$. Assuming inter-element spacing $d = \lambda_c/2$, the wavelength tuning range $\Delta\lambda$ required for the beam steering at azimuth φ and elevation θ angles is given as

$$\Delta\lambda = \frac{|\Delta\phi|}{2\pi \cdot D \cdot L_{SSMF} \cdot f_{RF}},$$

$$|\Delta\phi| = \begin{cases} \pi \sin(\varphi)\cos(\theta), & \text{in azimuth} \\ \pi \sin(\theta), & \text{in elevation} \end{cases} \quad (1)$$

This relationship holds for the aforementioned candidate mmWave generation schemes designed for wireless transmission at the carrier frequency f_c depicted in Fig. 2. Considering the relationship between the RF and the intermediate frequency (IF) at the optical modulator, we distinguish (a) electrical upshifting at the transmitter side (TEU), where $f_{RF}^a = f_{IF}$, and (b) optically assisted upshifting based on heterodyne photodetection (HDU), where $f_{RF}^b = f_{IF} + \Delta f_{OCG}$, and Δf_{OCG} is the frequency spacing between adjacent OCG tones. In both cases, we may consider two variants for the antenna site architecture, depending on the

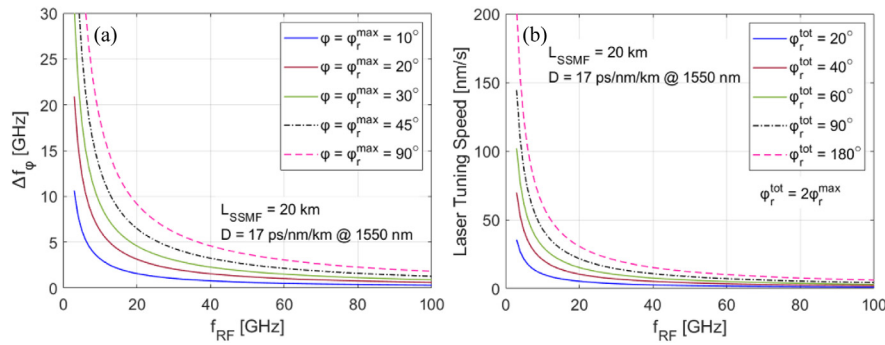


Fig. 3. (a) Optical tuning range requirement for the required azimuth steering angle φ_r^{\max} and (b) laser tuning speed v_{tun} needed for total angular coverage of φ_r^{tot} and $T_{SS} = 5$ ms, considering 20 km SSMF and C-band transmission.

relationship between the RF frequency and the intended air-interface mmWave frequency: (i) simplified RRH design (hereby referred to as RRH_S), where $f_c^{a,bi} = f_{RF}$, and (ii) electrical upshifting at the antenna side (denoted RRH_M), where $f_c^{a,bii} = f_{RF} + f_{LO}$, and f_{LO} is the electrical mixer frequency.

As shown in Fig. 2, assuming a ULA ($L = N$, $\theta = 0$), the required optical frequency tuning range Δf_φ for a given beam steering angle in CD-based OBFN systems exhibits an inverse dependence on the ARoF carrier frequency f_{RF} . This results from the wavelength-dependent mapping between RF phase progression and differential group delay in dispersive optical links. An increase in f_{RF} leads to progressively finer required phase shifts among the antenna elements, leading to reduced optical frequency spacing required to maintain a given steering angle. While this trend initially enables more compact spectral allocation for beamforming, the asymptotic behavior of this relationship yields diminishing benefits as the ARoF carrier frequency f_{RF} increases, which is relevant in scenarios where spectral efficiency must be weighed against other system-level trade-offs. In coexistence scenarios with legacy DWDM infrastructure, it is often more practical to treat the optical channel spacing Δf_φ as a fixed design constraint, dictated by standardized grid spacings. Under this premise, system optimization shifts toward identifying the minimum f_{RF} that enables the desired angular steering range while remaining within the fixed spectral allocation. This heuristic supports the identification of feasible trade-offs between spectral efficiency and implementation complexity, particularly where further reductions in Δf_φ are constrained by DWDM grid compatibility, increased impairment sensitivity, or photonic hardware limitations at higher RF frequencies. Finally, Fig. 3(a) shows that the resulting f_{RF} optimum acquired for a fixed Δf_φ is inherently use case dependent, as it varies with the steering angle requirement imposed by the intended beamforming application. As discussed, the basis for such optimization is the inclusion of electrical mixers at the antenna site, in use cases where it may be preferred compared to the TTD element distribution at the RRH or to the reliance on ultra-high bandwidth PDs and/or dedicated fiber transmission without consideration for optical spectrum constraints.

A baseline for time-domain beamforming requirements may also be established by following the 5G NR 3GPP-defined synchronization signal block (SSB) procedure [35], where

an SS burst covers the full angular range within $T_{SS} = 5$ ms. Considering the absence of DSP and assuming negligible beam management latency, while accounting for the fiber round-trip latency, the specified T_{SS} requirement would impose the minimum optical transmitter switching speed v_{tun} shown in Fig. 3(b). The choice of frequency spacing, once constrained by a fixed DWDM grid, affects the requirements placed on the tuning agility and spectral precision of the ARoF transmitters. Wider channel spacing necessitates faster tuning to accommodate dynamic beam steering with strict sweep latency requirements, while tighter spacing limits laser drift tolerance, imposing stricter stability and temperature control. Thus, the spectral requirements not only define the system architecture but also set critical performance benchmarks for ARoF transmitters in terms of tuning speed, precision, and long-term wavelength stability. The importance of thermal stabilization in λ -steered ARoF systems has been highlighted in experimental demonstrations such as [28], where lasers with 100 MHz stability and temperature control at the CO proved effective in keeping wavelength drift below 0.01 nm and preserving beamforming accuracy under realistic conditions. Regarding OFCs, wavelength stability better than 1 MHz has been employed to demonstrate tunable λ -to-AE beam steering capability [23]. Finally, temperature fluctuations in real-world deployments affect the fiber group delay, potentially affecting beamforming performance. Dynamic compensation strategies such as thermal stabilization, feedback-based λ -tuning adjustment at the CO, and periodic VDL calibration via the SSB procedure at the network control layer may be incorporated at the system level without affecting the core spectral feasibility principles discussed in this work. Although this work and its generalized system setup in Fig. 2 imply variability of delay lines at the RRH for completeness, such variability is not required if λ -tuning adjustments are handled at the CO. In that case, the RRH delay lines only serve for static rest state (i.e., boresight) calibration.

3. SYSTEM REQUIREMENTS UNDER THE SPECTRAL COEXISTENCE SCENARIO

It is critical to assess the conditions where CD-based beamforming schemes can coexist with legacy PON standards,

ensuring backward compatibility by confining their spectral occupation to optical bands not currently utilized. The currently active ITU-T standards include G-PON, video overlay for CATV, XGS-PON, NG-PON2, and 50G-PON, which jointly occupy the available optical spectrum across the C- and O-bands. However, as discussed extensively within the ITU-T VHSP initiative for future 200G-PON systems, the video overlay is now rarely deployed, and NG-PON2 never gained significant traction aside from limited adoption in the USA. Thus, there is a broad consensus within ITU-T that PON evolution should primarily account for G-PON, XGS-PON, and 50G-PON. As highlighted in [36], this assumption makes the 1500–1575 nm range, along with the >1580 nm region, available for emerging applications including the next-generation broadband use cases addressed in this paper. Provided that the ITU-T VHSP initiative adopts coherent PON, a portion of this range may become unavailable, though the specifics remain undefined. As a conservative estimate, we thus conclude that up to 30 nm within the C-band would likely remain available for ARoF λ -to-AE OBFNs. Such spectral planning would likely yield up to approximately 20–30 nm of potential usable bandwidth corresponding to 25–38 of supported channel slots representing the upper L limit, when considering 100 GHz DWDM grid in the above-defined C- and L-band ranges and depending on specific deployments. Assuming ITU-T Recommendation G.694.1 DWDM grids [37], commonly deployed in metro and long-haul systems, we consider the 100 GHz grid to be a suitable compromise for the OBFN applications analyzed in this paper, as it offers more relaxed filter and laser requirements compared to the 50 GHz option. A key constraint for such applications is aligning optical carriers to standardized WDM grids while preserving guard bands for filter roll-off and wavelength stability tolerances, limiting the ARoF channel tuning range and beamwidth. To scale the number of AEs in practical implementations, high-count OFCs have been explored. While our study does not analyze power budget constraints, it is important to note that fiber nonlinearities limit total launch power and must be considered in practical deployments. For reference, AF computations using measured fiber delays have been demonstrated without performance degradation from nonlinearities in setups of 90 channels at 25 GHz spacing over 13.1 km SSMF (5 dBm launch), 24 channels at 100 GHz over 10 km (2 dBm), 81 channels at 49 GHz over 2 km, and 36 channels at 25 GHz over 2 km [18,23,29,31].

A. Array Element Count Evaluation

To evaluate the feasibility of OBFNs under DWDM spectral constraints, we first established a method for the evaluation of the required ULA and UPA element count L . In order to calculate the number of required antenna AEs at a given carrier frequency f_c while considering various wireless link range d_{link} scenarios, we build on the link budget methodology in [38,39].

Key parameters, including the allowed subcarrier spacings (SCS), available channel bandwidths, FFT size, and target wireless spectrum utilization, are defined to determine the minimum subcarrier spacing Δf and the effective channel bandwidth B_c . In particular, we adopt a set of allowed channel

bandwidths B_c as in [40]. For a fixed FFT size of N_{FFT} points, a given bandwidth B_c , and a wireless spectrum utilization efficiency of η , the minimum subcarrier spacing Δf is then calculated using the methodology in [40]. This ensures that the selected N_{FFT} and wireless spectrum utilization target accommodate the channel bandwidth, as well as the $15 \cdot 2^\mu$ kHz base numerology defined in 3GPP [35], such that the smallest allowed subcarrier spacing is 15 kHz. For each numerology defined by the minimum subcarrier spacing, we then specify the supported channel bandwidths complying with the Nyquist criterion for the sampling frequency $f_s = N_{\text{FFT}} \cdot \Delta f$, ensuring alias-free signal reconstruction and compatibility with OFDM numerologies. Next, the channel bandwidth B_c is partitioned into a number of resource blocks (RBs), by dividing the effective channel bandwidth by the RB width of 12 subcarriers, $N_{\text{RB}} = B_c \cdot \eta / (12 \cdot \Delta f)$, while rounding down to ensure only full RBs are scheduled.

To consistently evaluate system performance across a wide f_c range, a uniform resource allocation of $N_{\text{RB}} = 261$ RBs is adopted in this work. This value results from the minimum considered bandwidth allocation set to $B_c = 50$ MHz, with $\Delta f = 15$ kHz and $\eta = 0.94$. This ensures that system comparisons are made on a common basis of total transmission resources, independent of the frequency band. To satisfy this constraint while respecting practical spectrum allocations, bandwidth-SCS pairs are selected based on the foreseen available bandwidth in each frequency range [40–42]. At lower frequencies, wireless spectrum availability is limited, favoring narrower bandwidths and smaller SCS values (e.g., 15 kHz with 50 MHz bandwidth at sub-3 GHz). As f_c increases, broader bandwidths become accessible, necessitating higher SCS to maintain the FFT size. In this work, the bandwidth and subcarrier spacing for each f_c are determined by fixing the N_{FFT} to 4096. This results in 261×12 subcarriers for all considered carrier frequency bands, similar to the scaling used in [38,40]. The adopted SCS and bandwidth settings per frequency range are summarized in Table 1.

The link budget is henceforth computed to characterize the achievable received signal-to-noise ratio (SNR) under realistic propagation and hardware constraints across the considered frequency range defined in Table 1 and with the above PHY layer specifications. In particular, the receiver SNR relationship to the total transmit power, the path loss, the receiver thermal noise power, as well as the transmitter (RRH) and receiver/user equipment (UE) antenna gains are modeled as in

Table 1. Bandwidth-SCS Pairs per Carrier Frequency Assuming $N_{\text{FFT}} = 4096$, $N_{\text{RB}} = 261$, and $\eta = 0.94$

Carrier Frequency Range ($f_c \in \mathcal{F}$)	Δf (kHz)	B_c (MHz)
450 MHz–3 GHz	15	50
3–6 GHz	30	100
7–14 GHz	60	200
15–50 GHz	120	400
51–70 GHz	240	800
71–100 GHz	480	1600
101–125 GHz	960	3200
126–150 GHz	1920	6400

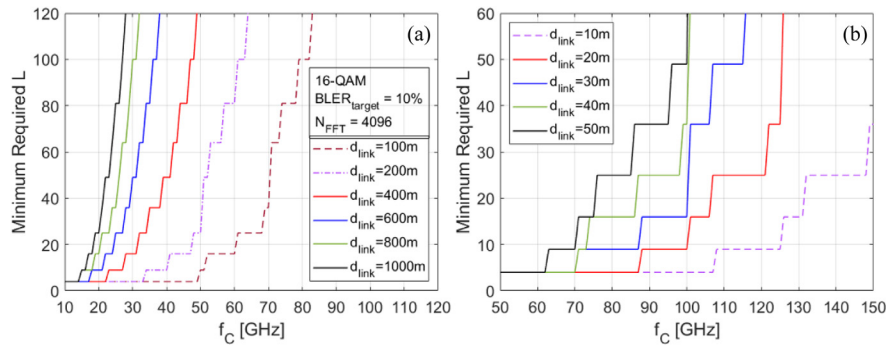


Fig. 4. Minimum required AE L , where $L = N^2$ when assuming $N \times N$ UPA, as a function of carrier frequency considering a varying coverage range (a) up to 1 km and (b) up to 50 m.

[39]. In this paper, a receiver noise figure (NF) of 10 dB and 290 K temperature for outdoor environments are adopted. In addition to free space path loss (FSPL) [39], we incorporate the atmospheric attenuation modeling targeting additional atmospheric propagation losses. The model accounts for dry-air absorption, which depends on environmental parameters such as temperature and pressure, as well as water vapor density effects that become significant at higher carrier frequencies [43]. For outdoor scenarios, rain attenuation is also included, with its severity determined by the local rain rate, using models specified in [44]. Furthermore, polarization mismatch between horizontal and vertical polarizations is also considered. In indoor deployment scenarios, rain attenuation and strong atmospheric gaseous absorption are hereby neglected. The available transmit power is modeled with a frequency-dependent back-off to reflect the physical limitations of power amplifier (PA) technology at high frequencies [40]. The rate of power decrease with frequency used in this paper is 1.5, whereas nominal transmit power and nominal frequency are set to 50 W and 1 GHz, respectively. This model captures a PA output power degradation of approximately 15 dB per frequency decade, consistent with empirical measurements and standard assumptions adopted in [45]. Next, our model assumes that the transmitter (RRH) and receiver (UE) antenna array elements are coherently combined, resulting in the effective RRH/UE gain equal to the individual element gain scaled by a factor of L . We hereby assume 3 dBi for the gain of a single AE.

Finally, to ensure the desired QoS levels, a block error rate (BLER) target is defined for each transmission block of size L_{block} (herein considered to be 8448 bits, the maximum LDPC code block size supported in 3GPP). The BLER is related to the underlying bit error rate (BER) through the approximation $\text{BLER} \approx 1 - (1 - \text{BER})^{L_{\text{block}}}$, where the relationship between the uncoded M-QAM modulation BER and SNR is modeled as in [46]. To enforce the QoS constraint for each considered f_c , the system calculates the RRH-to-UE wireless link distance d_{link} and antenna element count L pairs, ensuring the required SNR determined based on the modulation format and the target BLER. In this paper, the 16-QAM modulation along with the QoS requirement ensuring $\text{BLER} = 10\%$ is used, while the number of antennas at the UEs is kept fixed at 4. The results for the minimum required number of AEs L ($L = N^2$)

are presented in Fig. 4, showcasing the wireless link range limitations and the resulting beamforming criteria at a wide range of wireless carrier frequencies.

B. Spectral Coexistence Evaluation

To evaluate the feasibility of analog λ -to-AE OBFNs deployed over standardized DWDM grids in mmWave scenarios, a numerical method was developed to determine the maximum number of supported channels L conforming to a fixed grid spacing while satisfying system constraints. Our framework isolates spectral availability as the main constraint of interest, while specific signal-level ARoF transceiver characteristics and implementation are abstracted, with spectral impacts implicitly addressed through the allocation of optical guard bands (OGBs). We adopt a uniform DWDM grid with nominal channel spacing of $\Delta f_{\text{WDM}} = 100$ GHz. OGB bandwidth of $\pm B_{\text{OGB}}$ is reserved on each side of the ARoF signal spectrum to accommodate arbitrary filter roll-off, laser drift, and isolation margins. Following Section 2, for a given f_{RF} , the required optical tuning range Δf_{φ} is derived from the targeted angular steering range and fiber parameters. To account for practical uncertainties, such as the ± 10 nm zero-dispersion wavelength (ZDW) tolerance defined in ITU-T G.652, we conduct a parametric feasibility analysis over a realistic range of total dispersion $D \cdot L_{\text{SSMF}}$ values, while using Corning SMF-28 as a reference fiber model and ZDW within the 1302–1322 nm range. A dispersion slope of 0.09 ps/nm² · km is adopted to account for the third-order dispersion (TOD) contribution to the differential group delay. However, with VDL compensation applied in the rest state, residual TOD contribution to the differential phase error had a negligible impact on the beamforming gain in all use cases considered in this paper. In scenarios where the residual differential phase error reaches unacceptable limits, TOD may be compensated via λ -tuning adjustment [23] and accounted for with the B_{OGB} parameter. Spectral distribution supporting the required tuning range without adjacent channel OGB violation is then iteratively evaluated. The “rest state” of the spectral distribution aligns the channels to the centers of the DWDM grid, so that symmetric tuning is supported such that $\varphi_r^{\min} = -\varphi_r^{\max}$. The signal center frequencies are mapped to the grid positions, and spectral occupancy including OGBs is verified to avoid overlap. The framework output includes the maximum number of ARoF

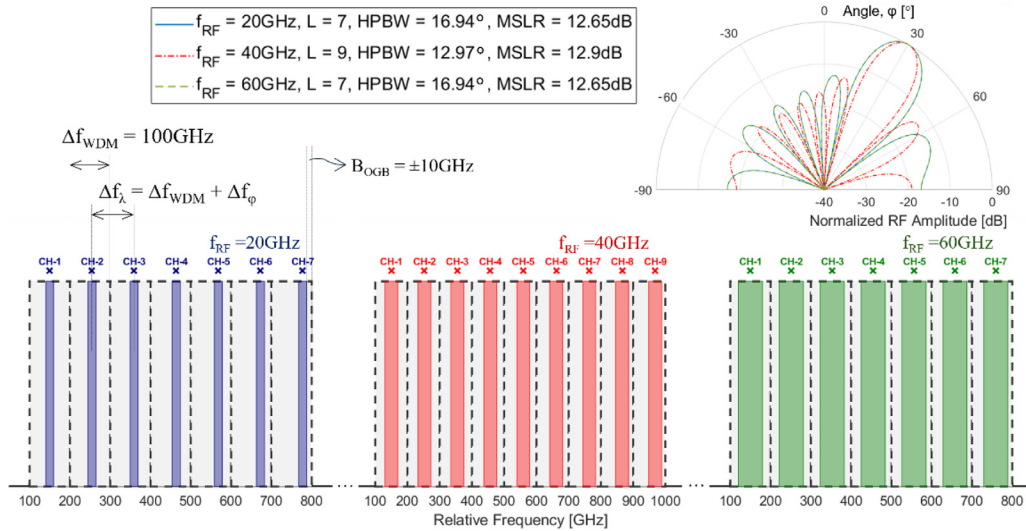


Fig. 5. Spectral distribution and radiation patterns for ARoF system architectures with f_{RF} set to 20 GHz (left, blue), 40 GHz (center, red), and 60 GHz (green, right), the resulting number of supported AEs L , HPBW, and MSLR. ARoF transmission using 20 km SMF-28 at $D = 17$ ps/nm/km, 100 GHz DWDM PON grid with $B_{\text{OGB}} = 10$ GHz, and $\theta = 0$ is considered.

signal replicas L , effectively representing the system angular resolution capability under the imposed grid and hardware constraints. Moreover, we calculate the resulting array factor (AF) to confirm the beam directivity and extract the half-power beamwidth (HPBW) and main-to-sidelobe ratio (MSLR) [32]. The minimum required ARoF transmitter tuning speed v_{tun} is evaluated considering the SSB procedure, as described in Section 2. Laser drift tolerance, Δf_{max} , is modeled as a perturbation in the central wavelength of each ARoF signal. In HDU architectures, the spacing between the radio signal and the LO tone f_{RF} is assumed unaffected, as both originate from the same laser per ARoF signal. The impact of laser drift is evaluated by computing the resulting differential phase shift perturbation among the ARoF signals, using the CD-induced delay expression from Section 2. Beamforming gain G_{bf} at the intended steering angles is modeled following the coordinate system and formalism in [32] and accounts for the resulting differential phase shifts across all ARoF signals. G_{bf} reduction due to drift-induced phase misalignment leading to the loss of constructive interference is then quantified. To estimate the worst-case degradation, a Monte Carlo approach is used: for a fixed $\pm \Delta f_{\text{max}}$, random signs of drift are assigned across ARoF signals in each trial. G_{bf} is computed for each configuration, and the minimum observed value across all trials is taken as the worst case. The number of trials is increased until convergence of the minimum G_{bf} ensures capture of the most destructive interference pattern. This process is repeated for multiple Δf_{max} values until maximum tolerable G_{bf} degradation is reached, calculated using methods in Section 3.A as the highest allowed loss that still maintains the minimum required L at given d_{link} and f_{RF} . This methodology enables quantitative assessment of spectral coexistence feasibility with legacy PON and informs design trade-offs between the spectral efficiency and beam steering requirements. Figure 5 illustrates the spectral distribution over a 100 GHz grid imposing limitation of L , reflected in radiation patterns for three characteristic cases

of f_{RF} . As discussed, f_{RF} may be optimized to maximize L in pursuit of increased HPBW requirements, while wireless transmission at f_c is achieved via the inclusion of electrical mixers with $f_{\text{LO}} = f_c - f_{\text{RF}}$ at the antenna site. The example showcased in Fig. 5 considers 20 km SMF-28 transmission with $D = 17$ ps/nm/km and $B_{\text{OGB}} = 10$ GHz. The insets focus on spectral distribution for φ_r^{max} , while channel spacing reduction in equal measure is supported for $-\varphi_r^{\text{max}}$.

As compared to the C-band, elevated dispersion in the L-band presents an opportunity for further expansion due to the reduced required tuning range. This requires L-band lasers, modulators, receivers, and optical amplifiers, while higher attenuation must be accounted for as well. Promisingly, recent advances in L-band optoelectronics, mostly driven by the multi-band trend in long-haul transport networks, have narrowed the performance gap with respect to the C-band [47–50]. Figures 6(a)–6(c) show the maximum number of supported ULA elements L over a 100 GHz DWDM grid considering SMF-28 at $D = 20$ ps/nm/km, with B_{OGB} set to ± 3 GHz. It showcases the relevance of f_{RF} optimization in maximizing the supported AE count. For an increased DL , the range of f_{RF} offering optimal beamforming performance narrows. Compared to 180° , the steering range of 60° (e.g., a “street canyon” scenario) nearly doubles the AE count L .

C-band allocation is preferred for component maturity and legacy compatibility but is only feasible in spectral windows unallocated to PON services. The L-band offers more spectral freedom but demands stricter design due to attenuation and less mature hardware. 100 GHz spacing best balances performance and grid alignment, while 50 GHz or denser grids may suit greenfield deployments or advanced filtering and stabilization setups [51]. Figures 6(d)–6(f) show L over a 100 GHz grid in the C-band, considering $B_{\text{OGB}} = \pm 3$ GHz. Evidently, in legacy coexistence scenarios, L-band ARoF transmission may become necessary in use cases requiring high beamwidth

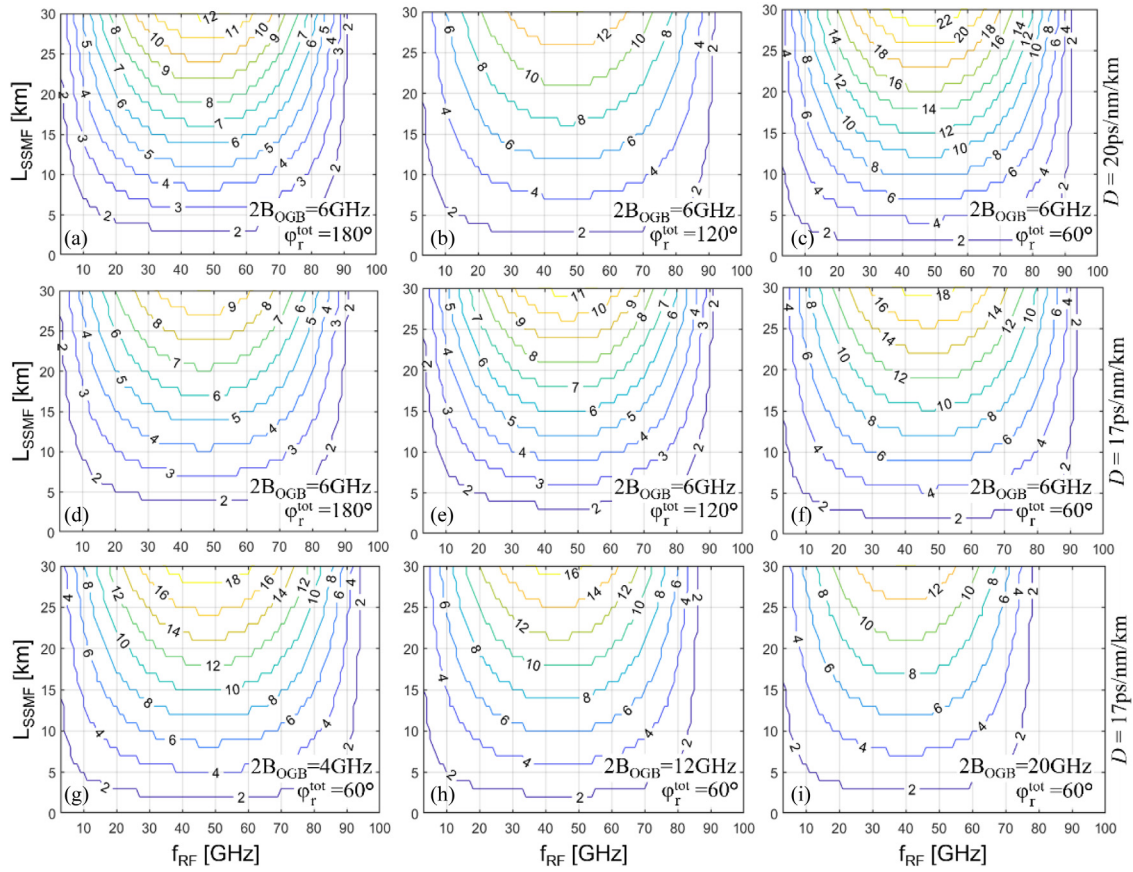


Fig. 6. Maximum supported L over a 100 GHz WDM grid as a function of f_{RF} and L_{SSMF} assuming $\theta = 0$ and required azimuth steering ranges of (a), (d) 180° ; (b), (e) 120° ; and (c), (g)–(i) 60° . $D = 20$ ps/nm/km (top), $D = 17$ ps/nm/km (middle and bottom), $2 \cdot B_{OGB} = 6$ GHz (top and middle), and (g) $2 \cdot B_{OGB} = 4$ GHz, (h) $2 \cdot B_{OGB} = 12$ GHz, and (i) $2 \cdot B_{OGB} = 20$ GHz are considered.

resolution, where unallocated C-band spectral availability becomes exhausted.

Figures 6(g)–6(i) show L over a 100 GHz DWDM grid in the C-band with varying B_{OGB} . The observed dependency of the optimal ARoF signal bandwidth on the configured B_{OGB} reveals a trade-off in spectral efficiency. The results for a fixed steering angle over 20 km of SMF-28 show that, as the B_{OGB} increases from 2 to 10 GHz, the optimal f_{RF} yielding the maximum number of non-overlapping signal replicas shifts from approximately 48 to 40 GHz. Expectedly, larger guard bands reduce the available bandwidth per DWDM slot, constraining the tuning range for each ARoF signal. Thus, ARoF fronthaul design must account for guard bands while relying on optimized spectral allocation strategies to maximize the resolution and scalability of ARoF-based beamforming systems within the limits of standardized grids.

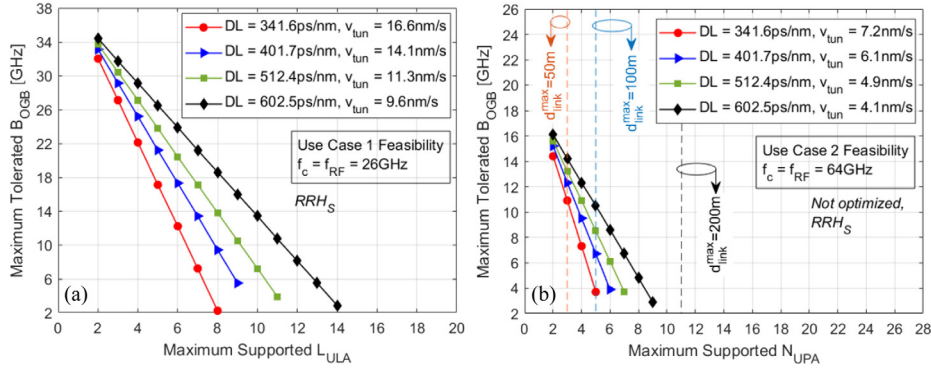
4. USE CASE ANALYSIS

In this section, we evaluate the per-use-case feasibility of analog λ -to-AE OBFN systems, relying on fiber CD and coexistence with legacy WDM-PON infrastructures, while considering the established antenna array density requirements in the mmWave range. Table 2 addresses the resulting wireless range and bandwidth for three characteristic use cases considering

the requirements for the (a) wireless carrier frequency range f_c , (b) antenna array element count L , (c) azimuth and elevation steering range φ_r and θ_r , and (d) latency. These requirements are set by using the following criteria. The frequency ranges are selected among those currently allocated to cellular services [52] or currently being considered [41]. Values for L ($L = N^2$ for a UPA) are derived using the methodology presented in Section 3.A. The choice between ULAs and UPAs is closely tied to the spatial characteristics of each use case. Steering range values are derived from typical deployment geometries and user movement patterns. For the latency requirement, the subcarrier spacing Δf directly influences the symbol duration ($T_{\text{symb}} = 1/\Delta f$), with larger spacings yielding shorter symbol durations. Since latency-sensitive applications require rapid transmission and fast scheduling, shorter symbol durations enable finer time granularity, making it possible to meet tight latency budgets through reduced transmission time intervals (TTIs). Although the mapping between SCS and specific latency requirements is illustrative, it reflects the aforementioned reasoning. The required laser tuning range and speed are calculated considering the SSB procedure requirements and fiber round-trip time, as explained in Section 2. Laser drift tolerance Δf_{max} is estimated as the maximum tuning error leading to beamforming gain degradation equal to the maximum loss allowed to keep L constant, as detailed in

Table 2. Summary of Per-Use-Case Requirements

Use Case	f_c (GHz) (a)	Configuration (b)	Steering (c)	Latency (d)	$d_{\text{link}}^{\text{max}}$	Bandwidth
FWA	24.25–28.35 (FR2-1)	ULA $L = 64$ –121	$\varphi_r = \pm 45^\circ$	≤ 10 ms (SCS 15 kHz or 30 kHz)	1 km	400 MHz
ER and HC	57–71 (FR2-2)	UPA $L = 16$ –64	$\varphi_r = \pm 60^\circ$ $\theta_r = \pm 30^\circ$	≤ 1 ms (SCS of 60 or 120 kHz)	100 m	800–1600 MHz
IH	37–48.2 (FR2-1)	UPA $L = 9$ –25	$\varphi_r = \pm 90^\circ$ $\theta_r = \pm 45^\circ$	≤ 5 ms (SCS of 30 or 60, 120 kHz)	200 m	400 MHz

**Fig. 7.** Maximum supported (a) L for FWA and (b) N ($L = N^2$) for RRH_S-based XR/HC use cases deployed over a legacy WDM grid versus B_{OGB} requirements for several DL values.

Section 3. We highlight that such estimation refers strictly to the beamforming system vulnerability to hereby addressed spectral limitations, whereas other contributions of laser drift to the ARoF segment SNR degradation are beyond the scope of this work. Based on these assumptions and methodologies, we highlight the following use cases and discuss their feasibility in the context of the spectral coexistence of the beamforming architecture depicted in Fig. 2 with legacy PON grids.

A. Fixed Wireless Access

Fixed wireless access (FWA) relies on mmWave frequencies to deliver high-speed broadband communications to homes and businesses, where the equipment is typically mounted on rooftops or towers to serve buildings spread in a horizontal fan. A ULA is thus the configuration of choice, as it provides directional gain and 1D steering, making it suitable for scenarios with static or planar user distribution such as FWA and smart factories. The assumption is that most customer premises will be located within a 90° (azimuthal) field of view.

Figure 7(a) shows the feasibility assessment results for several values of total dispersion DL and the resulting required tuning speed v_{tun} , while considering the criteria established in Table 2. The results showcase the number of supported $N \times 1$ ULA AEs ($L = N$), considering a range of allocated OGB constraints to emulate optical component spectral limitations. The results indicate that, to support up to 14 AEs, DL over 600 ps/nm is required along with ARoF transceiver equipment enabling stringent OGB allocation of ± 2 GHz and a minimum v_{tun} of 9.6 nm/s. As shown in Table 2, due to the high AE count requirement of $L = 64$, this use case is thus not feasible in 100 GHz DWDM grid coexistence scenarios. Therefore,

FWA requires a dedicated fronthaul feeder fiber when based on the λ -to-AE architecture depicted in Fig. 2.

When discarding the spectral constraints imposed by the scenarios of legacy coexistence over DWDM grids, considering a dedicated SMF-28 fiber with $L_{\text{SSMF}} = 20$ km and C-band allocation ($D = 17$ ps/nm/km), analog λ -to-AE OBFN system operating at $f_{\text{RF}} = f_c = 25$ GHz and relying on RRH_S architecture (i.e., with no electrical upshifting at the RRH) requires 10.4 GHz of total optical tuning range with 17.3 nm/s of transmitter tuning speed to provide 90° of total beam steering range, as confirmed by the results shown in Fig. 3.

B. Extended Reality and Holographic Communications

The extended reality (XR) and holographic communications (HCs) use cases support immersive applications like AR/VR and holographic calls, requiring ultra-high data rates and minimal latency. In contrast to FWA, UPA configuration is considered to enable 2D beamforming with finer angular resolution, better suited for dynamic and dense environments where users are distributed in both azimuth and elevation. Unlike FWA, XR requires user headset movement in all directions, demanding rapid beam tracking in both planes. $\pm 60^\circ$ azimuth provides wide horizontal freedom, while $\pm 30^\circ$ elevation accounts for seated/standing/leaning indoor users.

Figures 7(b) and 8(a) show the feasibility assessment results under the requirements presented in Table 2, while mapping the relationship between the wireless link range d_{link} requirements, presented in Fig. 4. The results showcase the number of supported per-dimension AEs N , assuming an $N \times N$ UPA

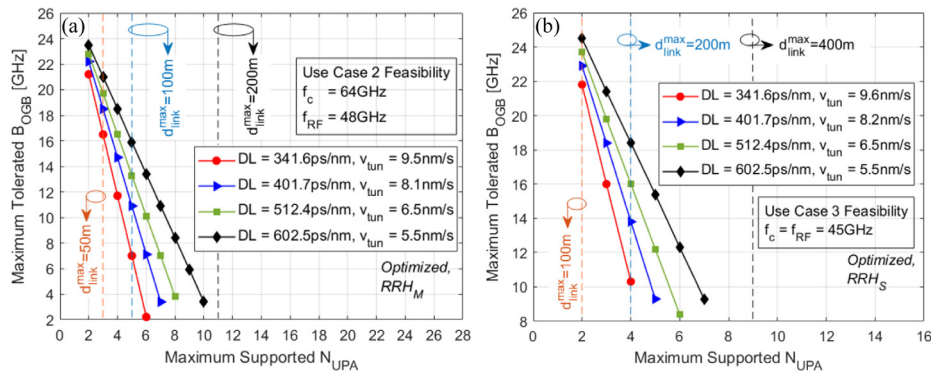


Fig. 8. Maximum supported N ($L = N^2$) deployed over legacy WDM grid versus the resulting B_{OGB} requirements for several DL values and (a) RRH_M -based XR/HC and (b) IH use cases.

($L = N^2$). We here consider both RRH_S and RRH_M architectures, as depicted in Fig. 2. As shown in Fig. 7(b), an ARoF system using a simplified RRH_S architecture may support $d_{\text{link}} > 100$ m only for $DL > 400$ ps/nm, with ARoF transceivers enabling $B_{\text{OGB}} = \pm 3.9$ GHz tolerance and a tuning speed v_{tun} of 6.1 nm/s. A UPA with 5×5 AEs is required to support a 100 m range, which at $DL = 341$ ps/nm imposes stringent $B_{\text{OGB}} = \pm 3.7$ GHz, $v_{\text{tun}} = 7.2$ nm/s, and Δf_{max} of 238 MHz. This use case showcases the impact of f_{RF} optimization enabled by RRH_M architecture relying on electrical mixers, as discussed in Section 3.B and shown in Fig. 8(a). In such a case, 100 m of d_{link} is feasible with relaxed guard band and drift requirements of $B_{\text{OGB}} = \pm 7$ GHz and $\Delta f_{\text{max}} = 359$ MHz at the expense of increased $v_{\text{tun}} = 9.5$ nm/s. Higher drift tolerance of the RRH_M architecture is the consequence of operating at lower f_{RF} , where larger channel detuning required per steering increment reduces sensitivity to tuning errors, as shown in Fig. 3(a). Moreover, as demonstrated in Fig. 8(a), lowering the transmission range d_{link} permits more considerable relaxation of system requirements in optimized RRH_M architectures.

C. Indoor Hotspot

The indoor hotspot (IH) use case (e.g., stadiums, malls) is characterized by dense user presence but more relaxed latency demands (real-time video or data download services). A UPA configuration is assumed, following the same environmental rationale as for XR. Access points are usually mounted above users, on ceilings or beams, needing full-circle horizontal coverage (i.e., $\pm 90^\circ$ azimuthal range). Stadiums or malls feature multi-level seating or escalators, requiring beams to point up/down in elevation; thus $\pm 45^\circ$ elevation value has been considered.

To benefit from the operation in the FR2-1 frequency range, we consider the deployment of this use case using a simplified RRH_S architecture, with no electrical upshifting at the antenna site. The feasibility assessment results for $f_c = 45$ GHz operation, showcasing the number of supported per-dimension AEs assuming an $N \times N$ UPA, are presented in Fig. 8(b). Wireless transmission over a 200 m range at 45 GHz requires $L = 16$. OBFN supports this range for all considered values of DL , with a clear trade-off between transmitter tuning stability, tuning speed, and system dispersion tolerance. Assuming

$DL > 400$ ps/nm, this use case is feasible considering ARoF transceiver equipment supporting $v_{\text{tun}} = 8.2$ nm/s and tolerating up to $B_{\text{OGB}} = \pm 14$ GHz. The calculated laser drift tolerances Δf_{max} for such a 4×4 UPA implementation considering $DL = 602.5$ ps/nm and $DL = 341.6$ ps/nm are 250 MHz and 451 MHz, respectively.

5. CONCLUSION

Due to the high path loss and directionality constraints of mmWave propagation, beamforming is essential for maintaining wireless link robustness, while system architectures based on ARoF fronthauling ensure a fully centralized low-latency, high-bandwidth solution. This paper addresses the feasibility of integrating such mmWave systems with legacy PON infrastructures, by examining the spectral compatibility of centralized λ -to-AE beamforming schemes that leverage fiber CD within standardized DWDM grids. We perform per-use-case feasibility assessment using a numerical framework developed for the evaluation of supported and required beamwidths while accounting for link distance, carrier frequency, and practical component and fiber coexistence constraints. We find that, in use cases operating beyond the FR2-1 band, RRH architectures incorporating electrical upshifting enable spectral efficiency optimization through the selection of ARoF carrier frequencies that meet beamforming requirements, while minimizing spectral demands under fixed DWDM grid constraints.

The feasibility analysis across three representative high-capacity mmWave access use cases, elected to broadly span fixed broadband, immersive communications, and dense indoor connectivity, highlights the impact of system dispersion, tuning speed, and ARoF transceiver capabilities under DWDM coexistence constraints. For FWA in FR2-1, high ULA element counts and wide steering angles necessitate dedicated fiber infrastructure due to the incompatibility with fixed dense WDM grids. For XR/HC in FR2-2, electrical frequency upshifting (RRH_M) enables critical carrier frequency optimization, supporting finer 3D beam control and stability tolerance with equal total dispersion. In IH scenarios, feasibility is achievable under broader dispersion tolerances without the need for frequency upshifting at the antenna site (RRH_S), although the beam steering resolution achieved depends strongly on the balance between the ARoF transmitter tuning

speed and optical guard band allocation. These results validate the need for use case-specific implementation strategies to ensure spectral coexistence under stringent beamforming requirements in practical deployments.

Funding. HORIZON EUROPE Marie Skłodowska-Curie Actions (101073265).

Acknowledgment. This work has received funding from the European Union's Horizon Europe research and innovation program under the Marie Skłodowska-Curie Actions (grant agreement no. 101073265, EWOC—"Enabling virtualized Wireless and Optical Coexistence for 5G and beyond"). Views and opinions expressed are, however, those of the authors only and do not necessarily reflect those of the European Union. The European Union cannot be held responsible for them.

REFERENCES

- J. Chen, X. Liang, J. Xue, *et al.*, "Evolution of RAN architectures toward 6G: motivation, development, and enabling technologies," *IEEE Commun. Surv. Tutorials* **26**, 1950–1988 (2024).
- C.-X. Wang, X. You, X. Gao, *et al.*, "On the road to 6G: visions, requirements, key technologies, and testbeds," *IEEE Commun. Surv. Tutorials* **25**, 905–974 (2023).
- H. Yang, W. Tian, J. Li, *et al.*, "Multi-band analog radio-over-fiber mobile fronthaul system for indoor positioning, beamforming, and wireless access," *Sensors* **25**, 2338 (2025).
- C. Ranaweera, C. Lim, Y. Tao, *et al.*, "Design and deployment of optical x-haul for 5G, 6G, and beyond: progress and challenges [Invited]," *J. Opt. Commun. Netw.* **15**, D56–D66 (2023).
- C. Lim, M. Tur, and L. Yaron, "Past and future development of radio-over-fiber," *J. Lightwave Technol.* **43**, 1525–1541 (2025).
- W. Hong, Z. H. Jiang, C. Yu, *et al.*, "The role of millimeter-wave technologies in 5G/6G wireless communications," *IEEE J. Microw.* **1**, 101–122 (2021).
- R. Rotman, M. Tur, and L. Yaron, "True time delay in phased arrays," *Proc. IEEE* **104**, 504–518 (2016).
- R. C. Hansen, *Phased Array Antennas*, 2nd ed. (Wiley-Interscience, 2009).
- H. J. Visser, *Array and Phased Array Antenna Basics*, 1st ed. (Wiley, 2005).
- B. Paul, K. Sertel, and N. K. Nahar, "Photonic beamforming for 5G and beyond: a review of true time delay devices enabling ultra-wideband beamforming for mmWave Communications," *IEEE Access* **10**, 75513–75526 (2022).
- S. Shi, H. Niu, W. Shi, *et al.*, "Integrated optical tunable delay line and microwave photonic beamforming chip: a review," *Laser Photonics Rev.* **19**, 2400663 (2025).
- X. Zhang, M. Zhao, Y. Jiao, *et al.*, "Integrated wavelength-tuned optical mm-wave beamformer with doubled delay resolution," *J. Lightwave Technol.* **38**, 2353–2359 (2020).
- Y. Meng, Y. Xiao, W. Li, *et al.*, "An up/downstream shared optical beam forming network for remote phased array antenna," *IEEE Photonics J.* **13**, 5500109 (2021).
- M. Burla, D. A. I. Marpaung, L. Zhuang, *et al.*, "Multiwavelength-integrated optical beamformer based on wavelength division multiplexing for 2-D phased array antennas," *J. Lightwave Technol.* **32**, 3509–3520 (2014).
- Y. Li, S. Ghafoor, M. F. U. Butt, *et al.*, "Analog radio over fiber aided C-RAN: optical aided beamforming for multi-user adaptive MIMO design," *Front. Commun. Netw.* **2**, 725976 (2021).
- Y. Liu, J. Yang, and J. Yao, "Continuous true-time-delay beamforming for phased array antenna using a tunable chirped fiber grating delay line," *IEEE Photonics Technol. Lett.* **14**, 1172–1174 (2002).
- H.-B. Jeon and H. Lee, "Photonic true-time delay for phased-array antenna system using dispersion compensating module and a multi-wavelength fiber laser," *J. Opt. Soc. Korea* **18**, 406–413 (2014).
- R. Liu, C. Zhang, X. Li, *et al.*, "Enhancing beamforming performance of microcomb-based optical true-time delay systems," *J. Lightwave Technol.* **43**, 3723–3730 (2025).
- X. Xue, Y. Xuan, C. Bao, *et al.*, "Microcomb-based true-time-delay network for microwave beamforming with arbitrary beam pattern control," *J. Lightwave Technol.* **36**, 2312–2321 (2018).
- M. Suga, Y. Takahashi, Y. Yamamoto, *et al.*, "2D pre-beamforming control method via analog radio over fiber for wireless communication systems with massive planar array antenna," *IEEE Access* **13**, 61760–61767 (2025).
- R. Oliveira, R. N. Nogueira, and M. V. Drummond, "Multi-beam microwave photonic beamforming based on self-coherent detection of a WDM signal," *J. Lightwave Technol.* **40**, 4956–4963 (2022).
- D. T. K. Tong and M. C. Wu, "Multiwavelength optically controlled phased-array antennas," *IEEE Trans. Microw. Theory Tech.* **46**, 108–115 (1998).
- X. Xu, J. Wu, T. G. Nguyen, *et al.*, "Photonic microwave true time delays for phased array antennas using a 49 GHz FSR integrated optical micro-comb source [Invited]," *Photonics Res.* **6**, B30–B36 (2018).
- J. L. Corral, J. Marti, and J. M. Fuster, "Optical up-conversion on continuously variable true-time-delay lines based on chirped fiber gratings for millimeter-wave optical beamforming networks," *IEEE Trans. Microw. Theory Tech.* **47**, 1315–1320 (1999).
- J. Yao, J. Yang, and Y. Liu, "Continuous true-time-delay beamforming employing a multiwavelength tunable fiber laser source," *IEEE Photonics Technol. Lett.* **14**, 687–689 (2002).
- D. B. Hunter, M. E. Parker, and J. L. Dexter, "Demonstration of a continuously variable true-time delay beamformer using a multi-channel chirped fiber grating," *IEEE Trans. Microw. Theory Tech.* **54**, 861–867 (2006).
- A. V. Marti, D. Loschenbrand, M. Hofer, *et al.*, "Photonic delay processing with centralized etalon cascade for radio beamsteering in simplified 2×5 phased-array radio heads," *J. Lightwave Technol.* **40**, 6929–6938 (2022).
- M. Oishi, T. Hirasawa, K. Furuya, *et al.*, "3.5-Gbit/s QPSK signal radio-over-fiber transmission with 60-GHz integrated photonic array-antenna beam forming," *J. Lightwave Technol.* **34**, 4758–4764 (2016).
- Y. Xie, M. Khalil, H. Sun, *et al.*, "Photonic beamforming using a quantum-dash optical frequency comb source," *Appl. Opt.* **62**, 8696–8701 (2023).
- J. Bohata, M. Komanec, J. Spáčil, *et al.*, "Experimental demonstration of a microwave photonic link using an optically phased antenna array for a millimeter wave band," *Appl. Opt.* **60**, 1013–1020 (2021).
- H. Huang, C. Zhang, C. Chen, *et al.*, "Optical true time delay pools based centralized beamforming control for wireless base stations phased-array antennas," *J. Lightwave Technol.* **36**, 3693–3699 (2018).
- E. Björnson and Ö. T. Demir, *Introduction to Multiple Antenna Communications and Reconfigurable Surfaces* (Now, 2024).
- B. J. Forman, "A novel directivity expression for planar antenna arrays," *Radio Sci.* **5**, 1077–1083 (1970).
- O. U. Omini, D. E. Baasey, and S. A. Adekola, "Impact of element spacing on the radiation pattern of planar array of monopole antenna," *J. Comput. Commun.* **7**, 36–51 (2019).
- 3rd Generation Partnership Project (3GPP), "5G; NR; physical layer procedures for control (release 17)," Technical Specification TS 38.213 V17.10.0 (3GPP, 2024).
- D. Nessel, "Progress on very high speed PON in ITU-T," in *Optical Fiber Communication Conference*, San Francisco, California, March 2025 (Optica Publishing Group, 2025), paper Th1J.5.
- "Spectral grids for WDM applications: DWDM frequency grid," ITU-T Recommendation G.694.1 (2020), <https://www.itu.int/rec/T-REC-G.694.1>.
- K. Rikkinen, P. Kyosti, M. E. Leinonen, *et al.*, "THz radio communication: link budget analysis toward 6G," *IEEE Commun. Mag.* **58**(11), 22–27 (2020).
- T. Schneider, A. Wiatrek, S. Preussler, *et al.*, "Link budget analysis for terahertz fixed wireless links," *IEEE Trans. Terahertz Sci. Technol.* **2**, 250–256 (2012).
- O. Tervo, I. Nousiainen, I. P. Nasarre, *et al.*, "On the potential of using sub-THz frequencies for beyond 5G," *arXiv* (2022).

41. International Telecommunication Union (ITU), "World Radiocommunication Conference 2023 (WRC-23): final acts" (2023), <https://www.itu.int/en/ITU-R/conferences/wrc/2023/Pages/default.aspx>.
42. 3rd Generation Partnership Project (3GPP), "Technical specification group radio access network; NR; 7–24 GHz frequency range (release 16)," 3GPP TR 38.820 V16.1.0 (2021), https://www.3gpp.org/ftp/Specs/archive/38_series/38.820/38820-160.zip.
43. "Attenuation by atmospheric gases," ITU-R Recommendation P.676-8 (2009), <https://www.itu.int/rec/R-REC-P.676-8-200910-S/en>.
44. Z. Zhao, M.-G. Zhang, and Z.-S. Wu, "Analytic specific attenuation model for rain for use in prediction methods," *Int. J. Infrared Millim. Waves* **22**, 113–120 (2001).
45. 3rd Generation Partnership Project (3GPP), "Radio frequency (RF) and co-existence aspects (release 14)," 3GPP TR 38.803 V14.4.0 (3GPP, 2024), https://www.3gpp.org/ftp/Specs/archive/38_series/38.803/38803-1440.zip.
46. K.-L. Du, *Wireless Communication Systems: From RF Subsystems to 4G Enabling Technologies* (Cambridge University, 2010).
47. C. Lei, H. Feng, Y. Messaddeq, *et al.*, "Investigation of C-band pumping for extended L-band EDFAs," *J. Opt. Soc. Am. B* **37**, 2345–2352 (2020).
48. J. Lang, C. Chen, P. Zhang, *et al.*, "C- and L-bands wavelength-tunable mode-locked fiber laser," *Photonics* **10**, 1379 (2023).
49. Y. Wang, B. Srivathsa, N. Tessema, *et al.*, "C and L band 1×12 AWG based on 3-μm SOI platform with 100 GHz channel spacing and low polarization sensitivity," in *Conference on Lasers and Electro-Optics*, San Jose, California (Optica Publishing Group, 2021), paper SW4E.7.
50. L. Wang, J. Zhang, J. An, *et al.*, "Ultra-broad bandwidth array waveguide grating for high-speed backbone network transmission," *Opt. Express* **31**, 37829–37842 (2023).
51. "40-gigabit-capable passive optical networks (NG-PON2): physical media dependent (PMD) layer specifications," ITU-T Recommendation G.989.2 (2019), <https://www.itu.int/rec/T-REC-G.989.2>.
52. 3rd Generation Partnership Project (3GPP), "5G; NR; base station (BS) radio transmission and reception," Technical Specification ETSI TS 138 104 V17.14.0 (ETSI, 2024), https://www.etsi.org/deliver/etsi_ts/138100_138199/138104/17.14.00_60/ts_138104v171400p.pdf.